# Lawrence Berkeley National Laboratory

**Title**

Nondissipative Martensitic Phase Transformation after Multimillion Superelastic Cycles

**Permalink**

https://escholarship.org/uc/item/8566j075

**Journal**

Physical Review Letters, 132(6)

**ISSN**

0031-9007

**Authors**

Karami, Mostafa

Zhu, Zeyuan

Chan, Ka Hung

et al.

**Publication Date**

2024-02-09

**DOI**

10.1103/physrevlett.132.066101

**Copyright Information**

Peer reviewed

# Non-dissipative martensitic phase transformation after multi-million superelastic cycles

Mostafa Karami,[1] Zeyuan Zhu,[1] Ka Hung Chan, [1,2]
Peng Hua, [1] Nobumichi Tamura, [2] Xian Chen [1*]

[1]Mechanical and Aerospace Engineering,
The Hong Kong University of Science and Technology, Clear Water Bay, Kowloon, Hong Kong
[2]Advanced Light Source, Lawrence Berkeley National Laboratory, California, United States

*To whom correspondence should be addressed; E-mail: xianchen@ust.hk.

**Superelastic alloys used for stents, biomedical implants, and solid-state cooling devices rely on their reversible stress-induced martensitic phase transformations. These applications require the alloy to sustain high deformability over millions of cycles without failure. Here we report an alloy capable of enduring 10 million tensile stress-induced phase transformations while still exhibiting over 2% recoverable elastic strains. The martensitic phase transformation becomes non-dissipative beyond millions of cycles without any nominal strain hardening. The long-lasting phase reversibility is achieved through the formation of compatible twins predicted by the geometric non-linear theory and confirmed by high-resolution TEM observations. Our results pave the way for the development of superelastic alloys for multi-million cycling applications in biomedical engineering and energy science.**

Alloys undergoing reversible solid-solid phase transformation possess two functionalities:

1

shape memory effect and superelasticity. The memory effect is achieved by thermally driven phase transformation, while the superelasticity is achieved by stress-induced phase transformation. These alloys are commonly known as shape memory alloys, used for smart actuators (*1*). They are also known as superelastic materials for their spontaneous deformation under the stress-induced phase transformation, widely applied in biomedical engineering, e.g. orthodontic wires and cardiovascular stents (*2, 3*), and energy science, e.g. solid-state refrigerators (*4, 5*). The emerging applications of these alloys require the recoverable strains to sustain over multi-millions stress-induced phase transformation cycles. Unfortunately, very rare transforming materials meet this requirement. The primary reason for the gradual loss of phase reversibility during cyclic transformations is the lattice mismatch at the interface between austenite and martensite. Under the cyclic stress-induced phase transformation, the recoverable strain degrades quickly, and strain hardening becomes prominent. For example, the most widely used shape memory alloy, Nitinol can only sustain 100 tensile cycles and 1000 compressive cycles (*6–8*). The fatigue life of Nitinol can be improved by microstructure engineering, such as grain refinement and morphological manipulation (*9, 10*), but these treatments cause severe local amorphization and lattice distortions that significantly increase the driving force for the superelastic strain. For example, the nanocomposite NiTi requires over 1 GPa stress to achieve 2% strain (*10*).

In recent years, new alloys have been developed to achieve a high fatigue resistance by the phase engineering methods (*11–14*). As a result, some superelastic thin films can reach 10 million cyclic fatigue life under stress-induced transformations (*13, 14*), some bulk alloys show extremely small thermal hysteresis (*15, 16*), more interestingly, some transforming functional ceramics shows singular transport properties with a high fatigue life (*17–19*). The key development criteria are known as Cofactor Conditions (CC) (*15*) including three sub-conditions CC1-3 (*16*). The thermal hysteresis is extremely sensitive to the CC1: $\lambda_2 = 1$ condition, where

$\lambda_2$ is the middle eigenvalue of the stretch tensor (*20*). As seen in Figure 1(a), a subtle decimal variation of $\lambda_2$, e.g. $1 \pm 0.005$, results in an increase of the thermal hysteresis by about a factor of 10. It was shown that the thermal hysteresis is minimized at $\lambda_2 = 1$ in many alloys and ceramics (*11, 12, 15, 17, 18, 21–23*). Naturally, it is believed that the phase reversibility can be simultaneously enhanced as $\lambda_2$ approaches 1, which was observed in some alloys (*12, 13, 22, 24, 25*). However, counter examples still exist. A superelastic alloy, $CuAl_{24}Mn_9$ (*26, 27*) exhibits an outstanding reversibility over 10k cycles of both tensile and compressive stress-induced transformations with $\lambda_2$ far away from 1. This suggests that the phase reversibility may not be fully entangled with the $\lambda_2 = 1$ condition, especially for the stress-induced phase transformation. The primary compatibility condition may be sufficient but not necessary to achieve high reversibility during stress-induced transformations. Figure 1(b) compares the stress hysteresis among martensitic alloys, in which behaviors of stress-induced transformations in some transforming alloys are not consistent with the thermal-driven transformation. It raises a question whether the $\lambda_2 = 1$ condition still dominates the phase reversibility of stress-induced transformation, especially over long-lasting mechanical cycles.

From a microstructure perspective, the CC1 condition suggests a twinless structure, i.e. the martensite forms as a single lath from the austenite through an atomically sharp interface (*32*). Although this microstructure is fully compatible, it limits the morphological flexibility to accommodate non-transforming defects during the phase transformation. For a stress-induced phase transformation, the formation of martensite variants is constrained by the loading orientation. As seen from Figure 1(b), the stress hysteresis varies by almost a factor of two as the loading orientation changes in $Ni_{50}Ti_{50}$ ([101] vs [111]) (*28*) and $CuAl_{24}Mn_9$ ([001] vs [111]) (*26*). It implies that the Gibbs free energy minimizers for the stress-induced phase transformation are orientation dependent, more specifically martensite variant dependent. During the axial loading, the formation of martensite variant should maximize the axial strain along
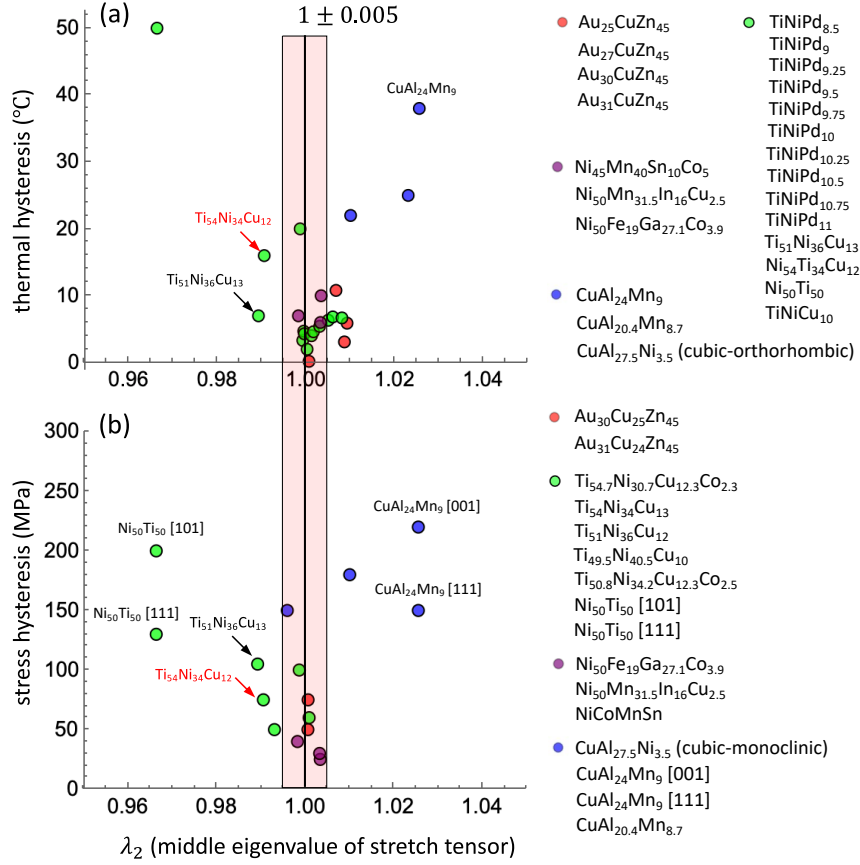
Figure 1: Relationship between the primary CC condition, $\lambda_2 = 1$ and (a) thermal hysteresis, (b) stress hysteresis, for CuZn based alloys from refs (*12, 24*) and this work, TiNi based alloys from refs (*15, 16, 22, 28*), Heusler alloys from refs (*21, 25, 29*) and CuAl based shape memory alloys from refs (*26, 30, 31*).

the loading direction, and minimize the lateral shear deformation to suppress slips. When the material satisfies the CC2 condition: $\mathbf{U}\mathbf{a} \cdot \mathrm{cof}(\mathbf{U}^2 - \mathbf{I})\mathbf{n} = 0$ where $\mathbf{a}$, $\mathbf{n}$ are the twinning parameters for the martensite variant $\mathbf{U}$, the morphological flexibility of compatible interfaces can be achieved by forming twin laminates with variable twinning volume fractions (*12, 16*). These compatible twins can accommodate local non-transforming defects, consequently the reversibility and functional stability over loading cycles can be enchanced.

In this paper, we explore the superelasticity and functional fatigue resistance over multi-million stress-induced phase transformations of the transforming alloy $Au_{31}Cu_{24}Zn_{45}$, belong-

ing to the compatible alloy family (*12*). The alloy development and theoretical calculations of Cofactor Conditions are provided in the Supplementary Materials. This alloy satisfies the CC1 condition with $\lambda_2 = 1.0067$ (not very close to 1) and CC2 condition with $\mathbf{Ua} \cdot \mathrm{cof}(\mathbf{U}^2 - \mathbf{I})\mathbf{n} = 0.000085$ (very close to 0) for $[1\bar{1}0]$ two-fold symmetry axis. Therefore, the martensite phase tends to form compatible twins rather than a single variant lath. To investigate the functional fatigue resistance, we carry out an in situ uniaxial tensile test on a T-shaped $Au_{31}Cu_{24}Zn_{45}$ micro-beam with width of 3 $\mu$m and thickness of 1.5 $\mu$m by FemtoTools Nanomechanical Testing System (model FTNMT03, Buchs ZH, Switzerland) under FEI Quanta 250 FEG Scanning Electron Microscope (SEM). We study the phase reversibility and stability of the alloy under stress-induced transformations, while observing the martensite formation and growth of structural defects. We conduct synchrotron X-ray Laue microdiffraction together with energy scans to characterize the loading orientation and precisely determine the lattice parameters of austenite and martensite near the transformation temperature at Beamline 12.3.2, Advanced Light Source, Lawrence Berkeley National Lab. Figure S2(a) in the Supplementary Materials gives the orientation map, from which we determined the out-of-surface normal vector as $\mathbf{t} = [0.09822, 0.48906, 0.8667] \approx [1\,5\,9]$ in terms of the cubic basis. This is considered as the uniaxial tensile loading direction. After long cyclic fatigue tests, we study the phase interfaces, twins and the non-transforming defects at the nano to atomic scales to explore the underlying mechanisms for the million-cycle reversibility.

Figure 2 shows the transformability and reversibility of the specimen under uniaxial tensile stress induced phase transformation up to 1 million cycles. During the first 100,000 tensile cycles, the transforming material is fully reversible. The stress-strain responses are almost identical without any nominal residual strains in Figure 2(a). The Supplementary Movie S1 shows a full superelastic cycle of the specimen under tensile stress-induced phase transformation. Based on the geometric non-linear theory of martensite with constraints (*20, 24, 26, 27*), we calculated
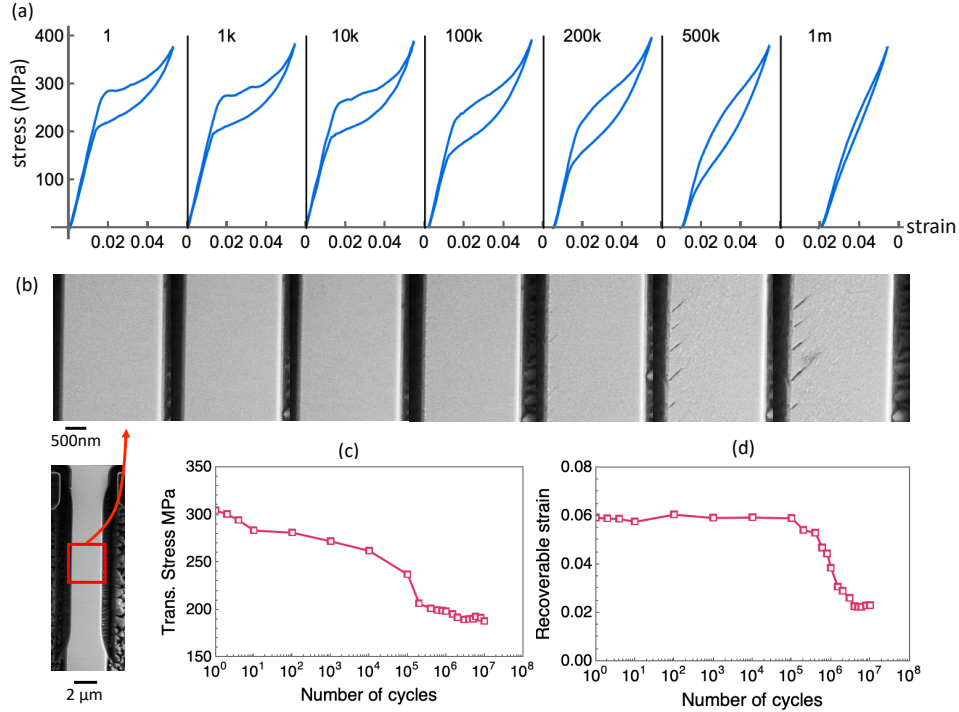
Figure 2: The superelasticity and the growth of the nanocracks in $Au_{31}Cu_{24}Zn_{45}$ up to one million tensile stress induced phase transformations. (a) Stress-strain behaviors of the micro-beam at the 1st, 1,000th, 10,000th, 100,000th, 200,000th, 500,000th and 1 millionth mechanical cycles, corresponding to (b) the lateral surface microstructure at the maximum tensile stretch. The functional degradation of the specimen is plotted for (c) transformation stress and (d) recoverable strain (i.e. superelastic strain) over number of cycles.

the compatible twin laminates, listed in Table S1 of Supplementary Materials, corresponding to the axial tensile strain $\epsilon_{cal} = 0.037$, which agrees with the superelastic strain, $\epsilon_{exp} = 0.034$ measured as the plateau strain shown in Figure 2(a). The transformation stress is determined as 300 MPa with about 80 MPa stress hysteresis corresponding to 4.5% total recoverable strains without degradation up to 200k transformation cycles.

As seen in Figure 2(b), the lateral surface is clean except for several nanoscale defect hubs on the left side of the specimen, which were nucleated from the 100k-th cycle. In subsequent tensile cycles, the specimen is loaded up to 400 MPa to complete the stress-induced transforma-

6

tion from austenite to martensite, then completely unloaded. Starting from the 200k-th cycle, we observed that the residual strain accumulates with increasing cycle number, while the superelastic strain and stress hysteresis are reduced. We observed that the superelastic behavior becomes less noticeable from the 500k-th to 1-millionth transformation cycles accompanied by an almost 90% decrease in stress hysteresis. Beyond this stage, we use the recoverable strain to represent the superelastic functionality. At the 1-millionth cycle, about 0.02 residual strain is accumulated due to the growth of nanocracks, recoverable strain still maintains almost 0.04, and the stress hysteresis almost vanishes. The Supplementary Movie S2 shows 40 consecutive cycles of tensile stress-induced transformations after 1 million cycles. From the in situ observation of the cyclic deformations (Movie S2), the specimen is still reversible and deformable with an output of 4% recoverable strain, while no conspicuous structural defects were observed on the lateral surface of the specimen.

Beyond one million cycles, we continued the mechanical tests on the $Au_{31}Cu_{24}Zn_{45}$ microbeam to obtain the stress-strain responses, associated with the growth of the nanocracks in Figure 3(a)-(b). From the 2-millionth cycle, the stress hysteresis became zero and the propagation of nanocracks in the specimen stopped. Figure 2(c)-(d) show that the stress-strain behavior converges, and over 0.02 recoverable strain was achieved and stabilized beyond million cycles. Strictly speaking, the mechanical behavior at this stage is not conventionally superelastic. The transformability of the tensile specimen remains quite promising with a total one-way work of $\sim 4$ MJ/m$^3$, estimated as the bulk elastic energy gained upon loading. As a comparison, the one-way work under tensile stress in NiTi (bulk) is 10 MJ/m$^3$, but it degrades to 5 MJ/m$^3$ after only 100 cycles (6). In magnetic shape memory alloys such as $Ni_2MnGa$, the one-way work in the first cycle is about 3 MJ/m$^3$ (33). This suggests that the compatible alloy is still functional even after 10 millions superelastic cycles. From SEM images of Figure 3(b), the structural defects were stabilized as the same microstructure was captured at 2, 4, 6, 8,10-millionth cy-
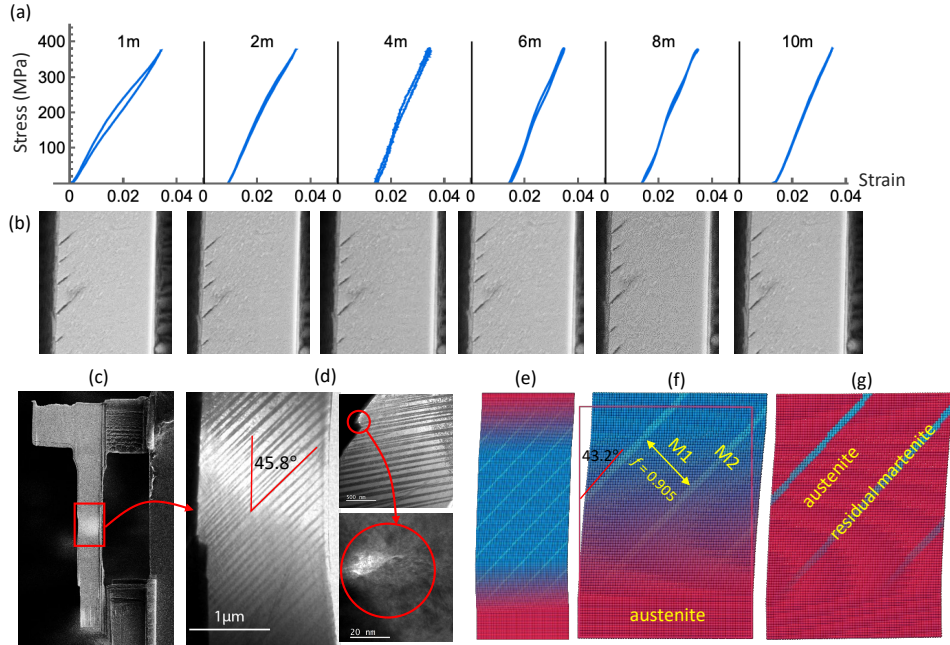
Figure 3: The transformability and reversibility of the $Au_{31}Cu_{24}Zn_{45}$ micro-beam beyond the million mechanical cycles. (a) Stress-strain responses under the tensile loading at the 1, 2, 4, 6, 8 and 10 millionth cycles, associated with (b) the grown nanocracks on the lateral surface. (c) The TEM foil fabricated for the (d) transmission electron microscope observation of the micro-beam after 10-million mechanical cycles. (e) Prediction of the formation of the compatible twin laminates with volume fraction of 0.905.

cles. The Supplementary Movie S3 shows 40 consecutive stress-induced transformations after 10 million cycles. The post-cycled micro-beam does not show nominal strain hardening, nor conventional slips even after numerous deformation cycles. The combination of large transformability and exceptional resilience provide a great potential for engineering applications in biomedical industries and energy science.

The post-cycled micro-beam was prepared for Transmission Electron Microscope (TEM) observations to study the mechanism responsible for the reversibility beyond million cycles. A tiny surface step was observed on the left side where the nanocracks nucleate. It suggests that the plasticity may have initialized during the cycling history. The open crack propagated along the laminates, then was closed after traveling a 20 nm distance. Signs of crossing slip lines
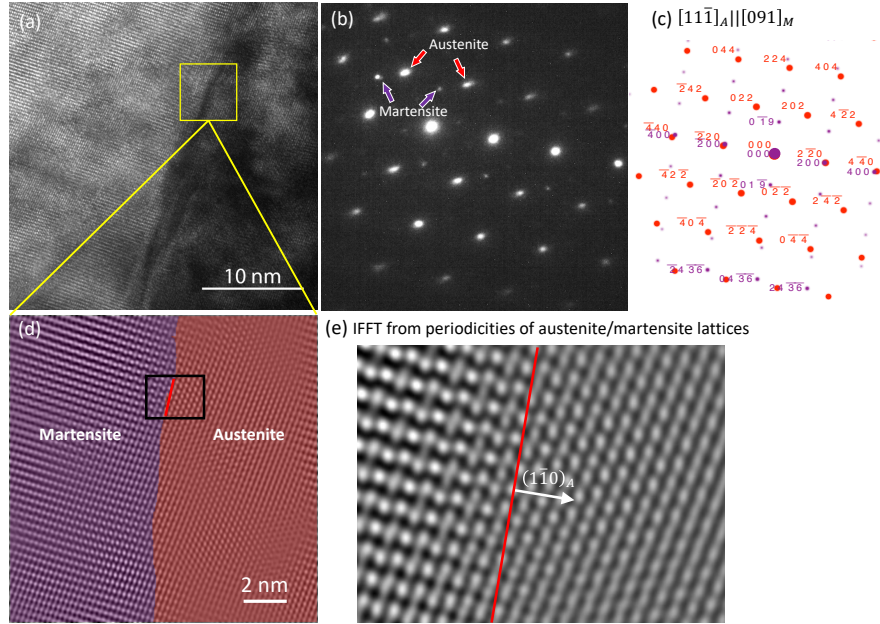
Figure 4: (a) High resolution TEM image of the post deformed specimen near the interface between laminates. (b) The diffraction patterns from the lattices on both sides (c) indexed by austenite (red) $Fm\bar{3}m$ symmetry and martensite (purple) $P2_1$ symmetry. (d) Resolved interface morphology with a zoomed reconstructed inverse Fourier transform of the austenite/martensite lattices.

were not observed in this specimen. Instead, Figure 3(c)-(d) suggests the presence of residual martensite phase. Based on the compatibility theory (*16, 20*), we calculate the compatible twin laminates shown in Figure 3(e)-(f). The details of the calculation are given in the Supplementary Materials. The calculated compatible twins consist of a major martensite variant M1 (dark blue) and a minor variant M2 (light blue) with a volume fraction 0.905 given in Figure 3(f). The transformation strain given by the minor variant of martensite is calculated as $\epsilon_{M2} = 0.0186$. Considering that about half of the region is occupied by the residual martensite (Figure 3 (d)), the minor variant M2 contributes to $\sim 0.01$ residual strain in the specimen. The transformation strain of the major variant M1 is $\epsilon_{M1} = 0.039$, corresponding to $\sim 0.02$ recoverable strain in the specimen. This calculation well agrees with the in situ nanomechanics experiment in Figure

9

3(a). It suggests that the minor variant is pinned while the major variant is still reversible after 10 millions of stress-induced transformation cycles.

In addition, we calculated the post-cycled microstructure of the austenite and residual martensite (i.e. M2 minor variant) in Figure 3(g). The calculated deformation field and the interfaces agree with the experimental observation in Figure 3(d). In our model, there is an elastic transition layer between austenite and the twinned martensite but the lattice distortion is very small, as the CC2 condition of this twin pair is closely satisfied, i.e. CC2 = 0.00085 for both type I and II twins with the two-fold axis $[1\bar{1}0]$. The numerical details are given in Table S1 of the Supplementary Materials. The vanishing of CC2 suggests a highly coherent interface in deformed configuration between austenite and martensite through normals of type I/II twinning planes, i.e. either $\mathbf{n}$ or $\mathbf{Ua}$. The calculated microstructure confirms such a high coherency at the austenite/M2 interface. To further verify the interface, we conducted the high-resolution TEM study (Figure 4(a)). The selected area diffraction patterns of the regions reveal that the two phases are austenite and a variant of martensite, as seen in Figure 4(b)-(c). The interface closely aligned with the $(1\bar{1}0)_A$ plane, corresponding to the $(100)_M$ plane. The phase contrast images from the selected sub-region of Figure 4(a) were reconstructed by fast Fourier transform and inverse Fourier transform (Figure 4(e)). We can clearly distinguish two periodicities from one side (austenite) to the other (martensite), and they are not mirror-symmetry related.

In addition, the CC2 condition ensures the flexibility of twin laminates morphology, the non-transforming defects can be accommodated during the stress-induced transformation. In both pre and post cycled specimen, the dislocation density is very low, verified by the TEM observations in Figure 3(c)-(d), 4(a) and Figure S3 in the Supplementary Material. The highly coherent interfaces satisfying the CC2 condition stabilize the nanocracks and other non-transforming defects. Beyond sufficiently many deformation cycles, the phase transformation has become non-dissipative. The observed residual strain is primarily attributed to the minor martensite

10

variant. The rest austenite region is still reversible because of the highly coherent and compatible interfaces between austenite and martensite. No further degradation will occur beyond this stage.
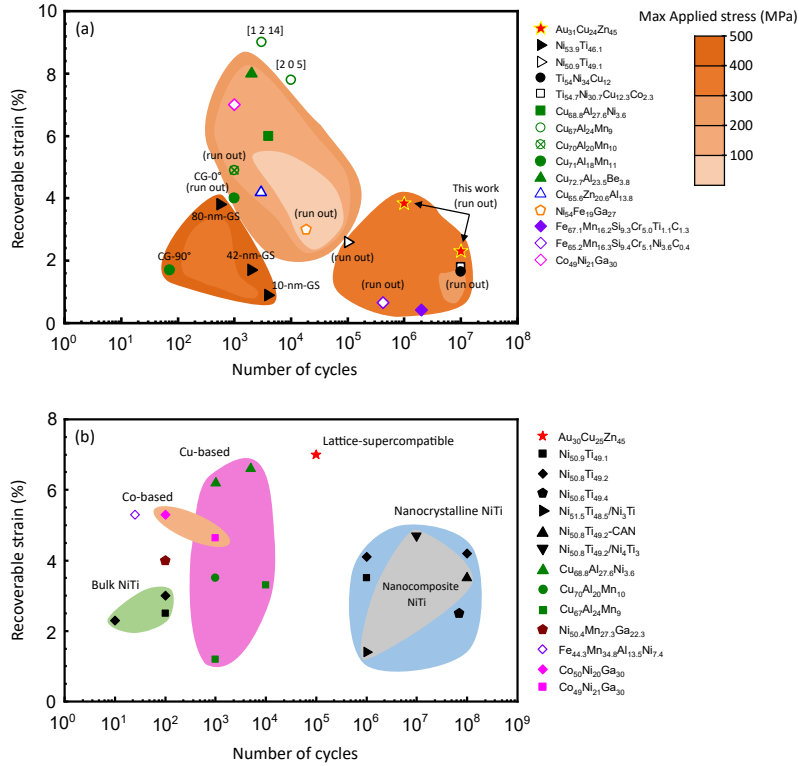


Figure 5: Comparison of the cycle-number dependent recoverable strain under (a) tension and (b) compression among common superelastic alloys such as NiTi based alloys (*7, 8, 10, 13, 34–41*), CuAl and CuZn based alloys (*8, 26, 27, 42–46*), FeNi-based alloys (*47–49, 49–51*), AuCuZn alloys (*24*). In (a), the contours of maximum applied stress during tensile cycling are overlaid. In (a) and (b): CG-0° and CG-90° stand for the columnar-grained tensile samples oriented in 0 and 90° to the solidification direction, respectively; GS refers to the grain size; and CAN stands for crystalline-amorphous nanocomposite. The details of the alloys and their corresponding references are listed in Supplementary Tables S2 and S3.

To conclude, we compared the recoverable strains of various transforming alloys under stress induced transformations in Figure 5. Overall, the fatigue resistance of alloys under tension is much lower than that under compression, while the achieved recoverable strains induced by tension are higher than by compression. The tensile loading is an effective actuation force but

is too demanding on superelastic alloys. In Figure 5(a), the cycle-number dependent property (i.e. recoverable strain) is overlaid by the maximum applied stress contours. The recoverable tensile strains of most superelastic alloys are about 4%. They can survive 1k $\sim$ 100k transformation cycles at 200-300 MPa applied stress. The compatible $Au_{31}Cu_{24}Zn_{45}$ alloy demonstrates the recoverable strain of 4% after 1-million cycles, and 2% beyond 10-million cycles. Note that this alloy was tested at a miniature size, in which the dislocations and non-transforming defects can easily slip across the specimen. But they are suppressed by the pinned martensite minor variant. A compatible superelastic thin film (*13*) was reported to show a comparable functional fatigue resistance, with less than 2% recoverable strain. In the benchmark of functional fatigue resistance under compression in Figure 5(b), the compatible $Au_{30}Cu_{24}Zn_{45}$ delivers the outstanding recoverable strain of 7% even after $10^5$ transformation cycles with no sign of functional degradation.

Through this comparison, we conjecture that the microstructure compatibility plays an unprecedented role in enhancing the reversibility of stress-induced phase transformation without causing strain hardening. Particularly, the satisfaction of the Cofactor Condition CC2: $\mathbf{Ua} \cdot \text{cof}(\mathbf{U}^2 - \mathbf{I})\mathbf{n} = 0$ allows for the compatible austenite and twinned martensite during the phase transformation. Moreover, it makes the lattice distortion in the elastic transition layer sufficiently small between austenite and residual martensite, stabilizing the non-transforming defect over the demanding deformation cycles. Beyond sufficient number of cycles, the phase transformation becomes non-dissipative. The non-dissipative nature of the stress-induced phase transformation under prolonged cycling ensures the exceptional resilience while maintaining the superelastic performance. Our findings provide a rational foundation for the design of superelastic materials for biomedical applications and energy science.

# References

1. K. Bhattacharya, R. D. James, *Science* **307**, 53 (2005).

2. T. Yoneyama, S. Miyazaki, *Shape memory alloys for biomedical applications* (Elsevier, 2008).

3. A. Biesiekierski, J. Wang, M. A.-H. Gepreel, C. Wen, *Acta biomaterialia* **8**, 1661 (2012).

4. E. Bonnot, R. Romero, L. Mañosa, E. Vives, A. Planes, *Physical review letters* **100**, 125901 (2008).

5. L. Mañosa, A. Planes, *Advanced materials* **29**, 1603607 (2017).

6. S. Miyazaki, T. Imai, Y. Igo, K. Otsuka, *Metall. Trans. A* **17A**, 115 (1986).

7. K. Otsuka, X. Ren, *Progress in materials science* **50**, 511 (2005).

8. M. Karami, X. Chen, *Materials Today Advances* **10**, 100141 (2021).

9. P. Hua, K. Chu, F. Ren, Q. Sun, *Acta Materialia* **185**, 507 (2020).

10. P. Hua, M. Xia, Y. Onuki, Q. Sun, *Nature Nanotechnology* **16**, 409 (2021).

11. J. Cui, *et al.*, *Nature materials* **5**, 286 (2006).

12. Y. Song, X. Chen, V. Dabade, T. W. Shield, R. D. James, *Nature* **502**, 85 (2013).

13. C. Chluba, *et al.*, *Science* **348**, 1004 (2015).

14. H. Gu, L. Bumke, C. Chluba, E. Quandt, R. D. James, *Materials Today* **21**, 265 (2018).

15. Z. Zhang, R. D. James, S. Müller, *Acta Materialia* **57**, 4332 (2009).

16. X. Chen, V. Srivastava, V. Dabade, R. D. James, *Journal of the Mechanics and Physics of Solids* **61**, 2566 (2013).

17. J. Jetter, *et al.*, *Physical Review Materials* **3**, 093603 (2019).

18. Y. Liang, *et al.*, *Nature communications* **11**, 1 (2020).

19. C. Zhang, Z. Zeng, Z. Zhu, N. Tamura, X. Chen, *Physical Review Applied* **16**, 024064 (2021).

20. J. M. Ball, R. D. James, *Arch. Rational Mech. Anal.* **100**, 13 (1987).

21. V. Srivastava, X. Chen, R. D. James, *Applied Physics Letters* **97**, 014101 (2010).

22. R. Zarnetta, *et al.*, *Advanced Functional Materials* **20**, 1917 (2010).

23. J. Liu, T. Gottschall, K. P. Skokov, J. D. Moore, O. Gutfleisch, *Nature materials* **11**, 620 (2012).

24. X. Ni, J. R. Greer, K. Bhattacharya, R. D. James, X. Chen, *Nano letters* **16**, 7621 (2016).

25. D. Zhao, *et al.*, *Acta Materialia* **133**, 217 (2017).

26. M. Karami, *et al.*, *Nano letters* **20**, 8332 (2020).

27. M. Karami, *et al.*, *Journal of the Mechanics and Physics of Solids* **160**, 104787 (2022).

28. R. Manjeri, S. Qiu, N. Mara, A. Misra, R. Vaidyanathan, *Journal of Applied Physics* **108** (2010).

29. Y. Li, *et al.*, *ACS applied materials & interfaces* **10**, 25438 (2018).

30. N. Zarubova, V. Novák, *Materials Science and Engineering: A* **378**, 216 (2004).

31. R. D. James, Z. Zhang, *Magnetism and structure in functional materials*, A. Planes, L. Mañosa, A. Saxena, eds. (Springer Berlin Heidelberg, 2005), pp. 159–175.

32. R. Delville, *et al.*, *Philosophical magazine* **90**, 177 (2010).

33. I. Karaman, *et al.*, *Scripta Mater.* **55**, 403 (2006).

34. H. Yin, Y. He, Z. Moumni, Q. Sun, *International Journal of Fatigue* **88**, 166 (2016).

35. J. Tušek, *et al.*, *Acta Materialia* **150**, 295 (2018).

36. R. Sidharth, A. Mohammed, H. Sehitoglu, *Shape Memory and Superelasticity* pp. 1–19 (2022).

37. H. Lin, P. Hua, K. Huang, Q. Li, Q. Sun, *Scripta Materialia* **226**, 115227 (2023).

38. P. Hua, H. Lin, Q. Sun, *Scripta Materialia* **203**, 114108 (2021).

39. J. Chen, K. Zhang, Q. Kan, H. Yin, Q. Sun, *Applied Physics Letters* **115**, 093902 (2019).

40. H. Hou, *et al.*, *Science* **366**, 1116 (2019).

41. F. Xiao, *et al.*, *International Journal of Plasticity* **160**, 103480 (2023).

42. J.-L. Liu, H.-Y. Huang, J.-X. Xie, *Materials & Design* **85**, 211 (2015).

43. C.-x. Qiu, S. Zhu, *Construction and building materials* **72**, 219 (2014).

44. S. M. Ueland, C. A. Schuh, *Acta materialia* **60**, 282 (2012).

45. J. F. Gómez-Cortés, *et al.*, *Acta Materialia* **166**, 346 (2019).

46. J. San Juan, J. Gómez-Cortés, G. López, C. Jiao, M. Nó, *Applied Physics Letters* **104**, 011901 (2014).

47. C. Efstathiou, H. Sehitoglu, P. Kurath, S. Foletti, P. Davoli, *Scripta materialia* **57**, 409 (2007).

48. K.-N. Hong, Y.-M. Yeon, W.-B. Shim, S.-W. Ji, *Applied Sciences* **10**, 5812 (2020).

49. P. Krooß, *et al.*, *Shape Memory and Superelasticity* **1**, 6 (2015).

50. L. Wei, X. Zhang, J. Liu, L. Geng, *AIP Advances* **8**, 055312 (2018).

51. A. Shen, D. Zhao, W. Sun, J. Liu, C. Li, *Scripta Materialia* **127**, 1 (2017).

# Acknowledgments

# Supplementary materials

Materials and Methods

Supplementary Text

Figs. S1 to S3

Tables S1 to S4

References *(1-30)*